Appl. Phys. B 74, 287–297 (2002)
DOI: 10.1007/s003400100688

Applied Physics B
Erratum **Lasers and Optics**

S. BERNHARDT[1]
H. VEENHUIS[2]
P. DELAYE[1,✉]
R. PANKRATH[2]
G. ROOSEN[1]

Effect of rhodium doping on the photorefractive properties of BCT crystals at 850 nm

[1] Laboratoire Charles Fabry de l'Institut d'Optique, Unité Mixte de Recherche, 8501 du Centre National de la Recherche Scientifique, Bat. 503, Centre Scientifique d'Orsay, B.P. 147, 91403 Orsay Cedex, France
[2] Universität Osnabrück, Fachbereich Physik, 49069 Osnabrück, Germany

Received: 23 May 2001
Published online: 7 February 2002 •

Appl. Phys. B **72**, 667–675 (2001)
DOI 10.1007/s003400100574
Published online: 30 April 2001

Due to a technical problem, lines in most of the figures for the original article were printed in a false form. Therefore here we print the complete article again in this erratum on the following pages.

✉ Fax: +33-1/6935-8700, E-mail: Philippe.delaye@iota.u-psud.fr

Appl. Phys. B 72, 667–675 (2001) / Digital Object Identifier (DOI) 10.1007/s003400100574

Applied Physics B
Lasers
and Optics

Effect of rhodium doping on the photorefractive properties of BCT crystals at 850 nm

S. Bernhardt[1], **H. Veenhuis**[2], **P. Delaye**[1,*], **R. Pankrath**[2], **G. Roosen**[1]

[1] Laboratoire Charles Fabry de l'Institut d'Optique, Unité Mixte de Recherche, 8501 du Centre National de la Recherche Scientifique, Bat. 503, Centre Scientifique d'Orsay, B.P. 147, 91403 Orsay Cedex, France
[2] Universität Osnabrück, Fachbereich Physik, 49069 Osnabrück, Germany

Received: 23 November 2000/Published online: 27 April 2001 –

Abstract. We present an experimental investigation of the photorefractive properties of rhodium-doped barium calcium titanate (BCT) crystals of the congruent melting composition $Ba_{0.77}Ca_{0.23}TiO_3$. Considering the results previously obtained on this crystal in the visible region, it should be a good alternative to $BaTiO_3$. Nevertheless, many applications use infrared light. Therefore we present here a study of rhodium-doped BCT crystals at 850 nm. This wavelength is of special interest as it is in the spectral range of laser diodes. Rhodium doping is expected to enhance the sensitivity of the crystal in the infrared as is the case for $BaTiO_3$.

We first noticed that BCT:Rh crystals are sensitive at this wavelength as expected. Furthermore, the photorefractive properties are interesting in terms of photorefractive gain, with a gain as high as 3 cm^{-1} with ordinary polarization. This study has also put forward the fact that rhodium is not the only defect that participates in the photorefractive effect. Indeed, a large quantity of iron seems to be present in the BCT crystals and to participate in the photorefractive effect.

PACS: 42.65 Hw; 77.84 S

It has been demonstrated that rhodium improves the infrared sensitivity of $BaTiO_3$ so that the crystal is of special interest for many applications. It exhibits high photorefractive gain, small response time and its behavior is well explained with a two-level model with three states of charges of rhodium: Rh^{3+}, Rh^{4+} and Rh^{5+} [1, 2]. But it suffers from a drawback that prevents its use in industrial systems: a phase transition around 5 °C, that can destroy it.

Recently, first results about a new ferroelectric crystal derived from $BaTiO_3$ with no phase transition at room temperature, $Ba_{0.77}Ca_{0.23}TiO_3$, were published and showed that this crystal has high electro-optic coefficients and high gain in the visible region [3–5]. As BCT is close to $BaTiO_3$, it is expected that rhodium will also improve the sensitivity of BCT in the infrared. BCT:Rh may thus be an alternative to $BaTiO_3$:Rh, provided its photorefractive properties in terms of response time, photorefractive gain and saturation intensity are good enough. Therefore, we will focus in this paper on the photorefractive properties of this new material at the near-infrared wavelength 850 nm. Absorption and two-beam coupling gain measurements are carried out in order to find out whether rhodium doping improves the photorefractive performances of BCT in the infrared.

*Corresponding author.
(Fax: +33-1/6935-8700, E-mail: Philippe.delaye@iota.u-psud.fr)

1 Experimental results

1.1 Crystals

BCT crystals grown with 0, 220, 370, 600, 1000, and 2000 ppm of rhodium added in the melt and one crystal with 140 ppm of iron are studied. Typical dimensions are $2 \times 3 \times 4$ (= c) mm^3.

The absorption spectra are presented in Fig. 1 (except for the 600-ppm rhodium-doped crystal for which the absorption spectrum was not measured). The influence of rhodium on absorption is the same as in $BaTiO_3$:Rh with a large absorption band around 600 nm which was attributed to this dopant [1, 6]. We can note in Fig. 1 that the absorption band seems to increase proportionally to the amount of rhodium added in the melt. To confirm this point, we normalized the absorption spectra to the quantity of rhodium added in the melt (Fig. 2a). To improve this comparison, we first substracted the absorption contribution of the undoped crystal from the ones of the rhodium-doped samples as we consider the absorption of the undoped BCT as a residual absorption present in all crystals. A departure from this assumption can explain the discrepancy between the curves in the short-wavelength part of the spectrum (400–600 mn). In the upper part of the spectrum, the low amplitude of the absorption background leads to a minor influence of the assumption except for crystals containing small amounts of rhodium (such as the 200 ppm rhodium-doped crystal for which the calculation is not performed). The similarity of the normalized absorption curves leads us to the conclusion that the observed absorption band is proportional to the rhodium doping.

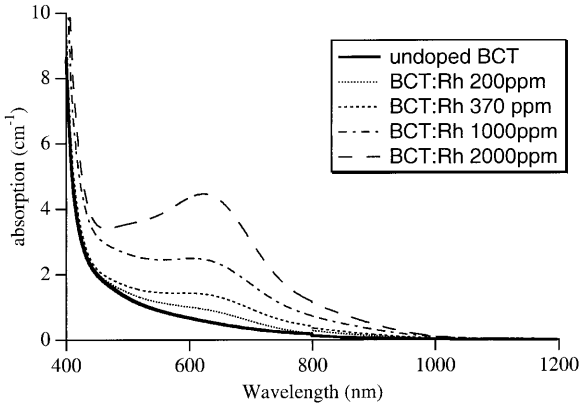

Fig. 1. Absorption as a function of wavelength for BCT:Rh crystals doped with different amounts of rhodium

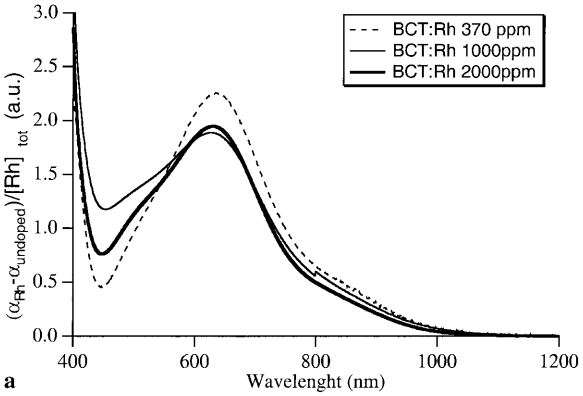

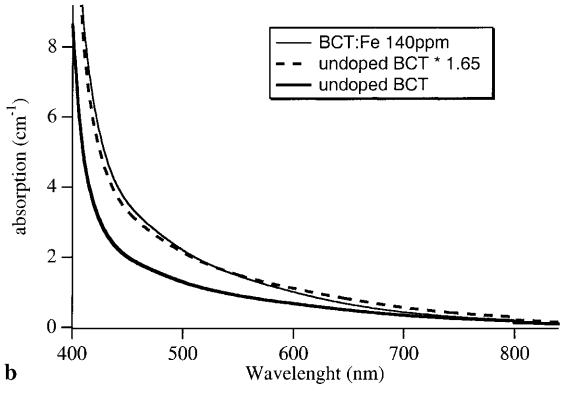

Fig. 2. a Absorption spectra of BCT:Rh from which we have subtracted the absorption of the undoped sample and divided by the amount of rhodium in the melt. **b** Absorption spectra for BCT:Fe and undoped BCT. The absorption spectra of the undoped crystal multiplied by 1.65 is almost identical to the absorption spectra of BCT:Fe

Moreover, we also see that the absorption spectra for the undoped and iron-doped crystals are similar. Indeed, as shown by Fig. 2b, both spectra are proportional, which certainly indicates the presence of iron in the undoped crystal.

1.2 Two-beam coupling experimental procedure

We carried out measurements of the photorefractive gain by using the two-beam coupling experimental arrangement shown in Fig. 3. Two coherent beams issued from a DBR laser diode at 850 nm were aligned so that the direction of the grating wave vector made an angle β with the c-axis of the crystal. All the experiments (with the exception of the measurement of r_{42}^{T}) are performed with ordinary polarizations and with symmetric incidences of the beams ($\beta = 0$). The choice of the ordinary polarization enables us to measure moderate energy transfers and thus prevents us from any measurement problems due to depletion of the pump beam, beam fanning or oscillation of beams inside the crystal that often occurs with extraordinary polarizations. The signal-beam diameter was reduced compared to the one of the pump beam by passing through a hole H to ensure a good overlap between the two beams. Furthermore, the intensity of the signal beam was much less than the one of the pump beam (a factor of 100) in order to be in the undepleted pump approximation. From the steady-state intensities of the transmitted signal beam without (I_{S}) and with (I_{SP}) illumination by the pump beam, we calculated the two-beam coupling coefficient Γ according to (1):

$$\Gamma = \frac{1}{l} \ln \left(\frac{I_{\mathrm{SP}}}{I_{\mathrm{S}}} \right) \tag{1}$$

where l is the length of interaction between the two beams, which corresponds here to the length of the crystal. Each measurement datum corresponds to a measurement in attenuation and in amplification allowing us to separate the photorefractive components from an eventual absorption contribution (induced absorption or absorption grating). We measured the dependence of the gain with several parameters: intensity of the pump beam, grating wave vector, angle between the c-axis and the grating wave vector β.

1.3 Theoretical aspect

The dependence of the gain with the grating wave vector $\boldsymbol{k}_r$ and with intensity I can be most of the time described by a general expression of the form [7–10]:

$$\Gamma = \frac{2\pi}{\lambda_0} n^3 \frac{k_{\mathrm{B}} T}{e} r^{\mathrm{eff}} \eta(I) \frac{k_r}{1 + \frac{k_r^2}{k_0^2(I)}} \tag{2}$$

where λ_0 is the wavelength of light in vacuum, n the mean refractive index and r^{eff} the effective electro-optic coefficient.

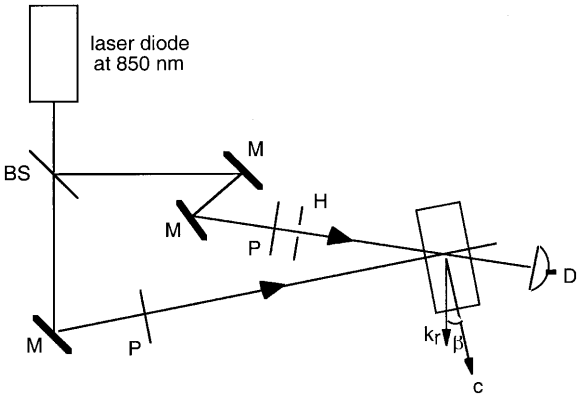

Fig. 3. Experimental setup for two-beam coupling experiments with copropagating waves; M: mirror, BS: beam splitter 50/50, H: hole, P: polarizor, D: detector

In this expression, $\eta(I)$ expresses the saturation of the gain with intensity which generally can be written as:

$$\eta(I) = \frac{1}{1 + \frac{I_{\text{sat}}}{I}} \tag{3}$$

and k_0 is expressed as a function of the effective trap density N_{eff} according to (with the effective dielectric constant $\varepsilon^{\text{eff}}(\beta)$):

$$k_0^2(I) = \frac{e^2 N_{\text{eff}}(I)}{k_B T \varepsilon_0 \varepsilon^{\text{eff}}(\beta)} \ . \tag{4}$$

On the one hand, the saturation of the gain is physically linked to the respective amplitudes of the photoconductivity and the dark conductivity, $\eta(I)$ approaching one for illumination, at which point photoconductivity surpasses the dark conductivity. On the other hand, the intensity dependence of the effective trap density is due to the charge redistributions that can occur among different photorefractive species. Using the expressions (1)–(4) to adjust our experimental results, we will deduce three characteristic parameters of the crystals: the effective electro-optic coefficient, the saturation intensity and the effective trap density. These parameters will enable us to compare the different crystals.

1.4 Experimental results

1.4.1 Gain as a function of intensity. The intensity dependence of the gain gives information about the intensity necessary to saturate the gain. It is a very important parameter for some applications, such as phase conjugation, that have a photorefractive gain threshold and where a decrease of the gain can prevent passing this threshold. The intensity dependence of the gain will allow the determination of the power of the laser source that will be necessary to implement such a device. This problem has to be considered especially in the infrared because the photoconductivity of materials such as BCT decreases. We fixed the grating spacing at $1.5\,\mu\text{m}^{-1}$, which implies that we have $k_r^2 \ll k_0^2$, leading to a dependence given by:

$$\Gamma(I) = \eta(I)\Gamma_\infty = \frac{\Gamma_\infty}{1 + \frac{I_{\text{sat}}}{I}} \tag{5}$$

where $\Gamma_\infty = \frac{2\pi}{\lambda_0} n^3 r^{\text{eff}} \frac{k_B T}{e} k_r$ is the saturated gain. Experimentally, I_{sat} is the intensity necessary to reach half of the maximum gain.

By fitting the experimental results according to (5) and Fig. 4a, we deduce the values of the saturation intensity for each crystal (Table 1). In Fig. 4a, the saturated gain Γ_∞ is normalized to 1 in order to enable the comparison of the curves. First, we noticed that the saturation intensity decreases when the quantity of rhodium in the crystals goes from 0 to 2000 ppm. Furthermore, the saturation intensity of the iron-doped crystal is the highest. Second, we noticed that the saturation intensity for the BCT:Rh crystals is between 100 and 1000 time higher than for $BaTiO_3$:Rh. Indeed, we measured the saturation intensity for a $BaTiO_3$:Rh crystal with 2000 ppm of rhodium (labelled Y32-B) and we found 0.5 mW cm^{-2}. It means that we need 100 to 1000 times more intensity to saturate the gain of a BCT:Rh crystal than for a $BaTiO_3$:Rh crystal if the crystals are doped with the same amount of rhodium.

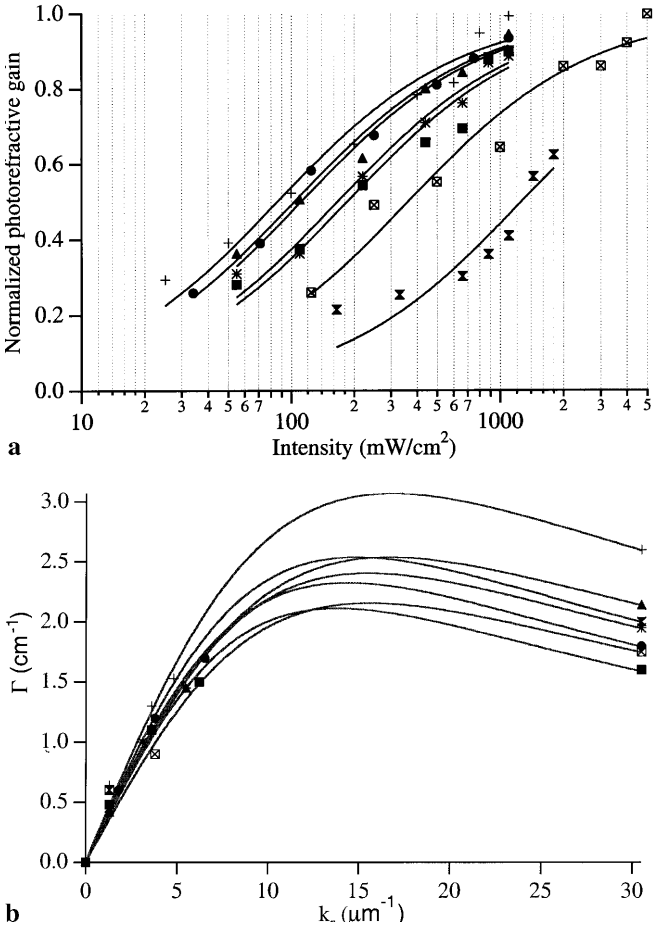

Fig. 4. a Normalized photorefractive gain as a function of intensity. **b** Photorefractive gain in ordinary polarization as a function of the grating wave vector. In both figures, the *points* correspond to experiments and the *lines* corresponds to the *fitting curves*. ⊠ undoped BCT; ■ BCT:Rh 200 ppm; ✳ BCT:Rh 370 ppm; ▲ BCT:Rh 600 ppm; ● BCT:Rh 1000 ppm; + BCT:Rh 2000 ppm; ⧗ BCT:Fe 140 ppm

Table 1. Values of the saturation intensity, the effective trap density and the effective electro-optic coefficient determined for all studied crystals

Crystal	I_{sat} (mW/cm^2)	N_{eff} (m^{-3})	r_{22}^{eff} (pm/V)
BCT:Fe 140 ppm	1300	5.4×10^{22}	15
undoped BCT	360	6.2×10^{22}	11.6
BCT:Rh 200 ppm	190	4.9×10^{22}	12.8
BCT:Rh 370 ppm	170	6.1×10^{22}	13
BCT:Rh 600 ppm	110	7.1×10^{22}	12.8
BCT:Rh 1000 ppm	100	5.3×10^{22}	13.6
BCT:Rh 2000 ppm	90	7.2×10^{22}	15.3

1.4.2 Gain as a function of the grating wave vector. Measurements of the gain as a function of the grating wave vector are carried out to determine the effective electro-optic coefficient and the effective trap density of the crystals. The measurements are performed with an intensity sufficient to saturate the gain, determined according to the previous measurements.

Then, according to (2), the photorefractive gain is expressed as:

$$\Gamma = \Gamma_\infty = \frac{2\pi}{\lambda_0} n^3 \frac{k_B T}{e} r^{\text{eff}} \frac{k_r}{1+\frac{k_r^2}{k_0^2}} \ . \tag{6}$$

Two kinds of measurements were performed. First, using the arrangement shown in Fig. 3, we measured the two-beam coupling gain with copropagating waves. In this configuration, for $\beta = 0$, we performed measurements at small grating wave vector ($k_r^2 \ll k_0^2$). According to (6), we have:

$$\Gamma \approx \frac{2\pi}{\lambda_0} n^3 r^{\text{eff}} \frac{k_B T}{e} k_r \ . \tag{7}$$

The linear dependence of the gain with the grating wave vector enables us to determine the effective electro-optic coefficient but will not give a precise value of the effective trap density, which appears as a departure from the linear curve at high value of k_r. To determine the effective trap density, we carried out another measurement in the configuration presented on Fig. 5, i.e. with counterpropagating beams [7]. In this particular case, with a large grating wave vector ($k_r^2 \gg k_0^2$), the gain is dominated by k_0^2 (i.e. the trap-limited field E_q defined in a one-trap model [10]) and this measurement enables us to evaluate the effective trap density according to (4).

No experimental points are given between 7 and 30 μm^{-1} because these values of grating wave vector are either forbidden due to refraction laws (14–30 μm^{-1}) with the crystal cut we used, or correspond to large angles between the beams, which leads to problems for the beams to overlap in the whole crystal (7–14 μm^{-1}). Nevertheless, the conjugation of copropagative ($k < 10\,\mu m^{-1}$) and counterpropagating ($k \approx 30\,\mu m^{-1}$) measurements is sufficient to determine precisely the effective trap density [7].

We performed then a simultaneous fit with two parameters on the measurements with copropagating and counterpropagating waves (Fig. 4b) using a function of the type $\Gamma = A r^{\text{eff}} \frac{k_r}{1+\frac{k_r^2}{k_0^2}}$ (A is a known constant). We obtained the effective electro-optic coefficient r^{eff} and the parameter k_0^2 from which we deduced the effective trap density (4) using the value of $\varepsilon^{\text{eff}}(0)$ calculated in [4] ($\varepsilon^{\text{eff}}(0) = 181$). In the configuration of the experiment, the effective electro-optic coefficient is $r_{22}^{\text{eff}}(0)$ and is expressed as:

$$r_{22}^{\text{eff}}(0) = r_{13}^{S} + \frac{p_{13}^{E} e_{33}}{c_{33}^{E}} \tag{8}$$

if we consider the indirect electro-optic contributions (elasto-optic, elastic and piezo-electric) [4].

In a simpler way, the effective trap density is deduced from the maximum of the curves presented in Fig. 4b and the effective electro-optic coefficient is given by the slope of the curves at small grating wave vectors. From the fit, we obtained an almost constant value $N_{\text{eff}} = (6 \pm 2) \times 10^{22}\ m^{-3}$ whatever the crystals (Table 1), whether they were rhodium-doped from 200 to 2000 ppm, iron-doped or undoped. The mean the value of the electro-optic coefficient is $r_{22}^{\text{eff}} = (13.5 \pm 1.3)\ pm\,V^{-1}$ (Table 1).

1.4.3 Dependence of the effective trap density on intensity. We also measured the dependence of the effective trap density on intensity on a 1000-ppm rhodium-doped crystal. The experimental conditions are similar as for the previous measurements presented in Sect. 1.4.2. This time, we carried out measurements of the gain as a function of the grating wave vector for several intensities. These intensities were chosen in a range so that the gain depended on intensity. We chose intensities of $2\,W\,cm^{-2}$, $200\,mW\,cm^{-2}$ and $50\,mW\,cm^{-2}$. We see in Fig. 6 that the position of the maximum of the curves, which corresponds to the effective trap density, depends on the intensity in the chosen range. Adjustments performed as explained in Sect. 1.4.2 enable us to determine the effective trap density for each laser intensity. The results presented in Table 2 show a dependence of the effective trap density on intensity.

1.4.4 Determination of r_{42}^{T}. The experimental configuration for the determination of the unclamped value of the electro-optic coefficient r_{42}^{T} is presented in Fig. 3 with a crystal oriented such that the grating wave vector is perpendicular to the

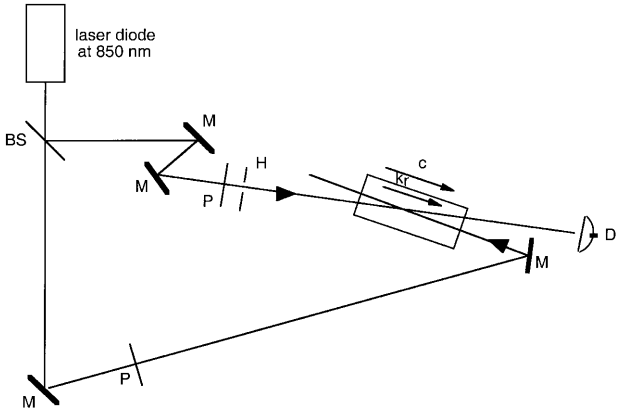

Fig. 5. Experimental setup for the measurement of the gain with counterpropagating waves

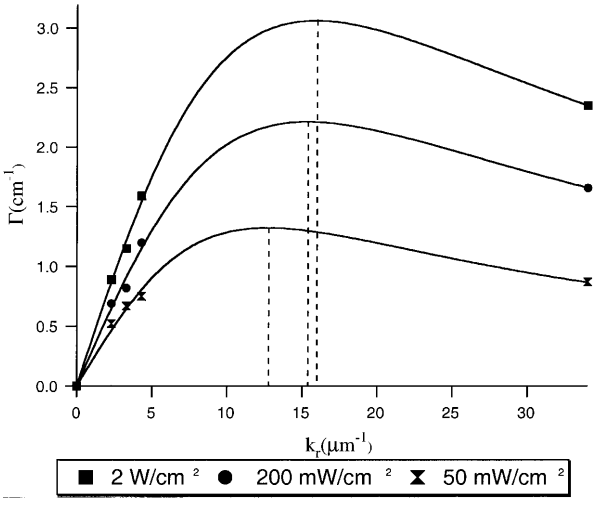

Fig. 6. Dependence of the gain with the grating wave vector for several laser intensities for a 1000-ppm rhodium-doped BCT crystal

Table 2. Dependence of the effective trap density and of the saturation coefficient η on intensity for a 1000-ppm rhodium-doped BCT

Intensity (W/cm^2)	Effective trap density (m^{-3})	$\eta(I)$
2	6.5×10^{22}	1
0.2	5.9×10^{22}	0.75
0.05	4.1×10^{22}	0.54

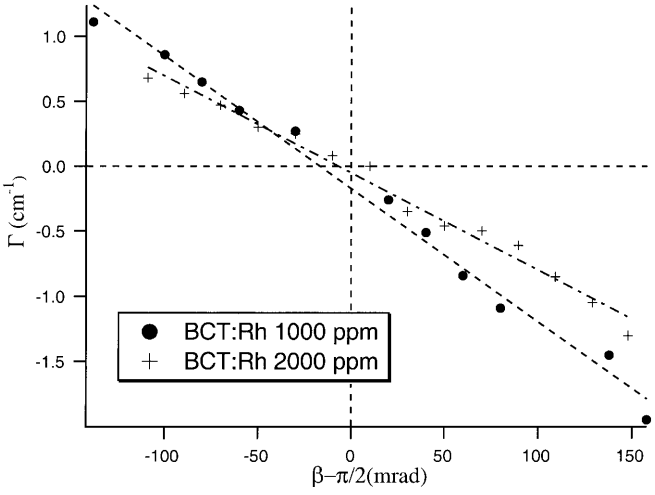

Fig. 7. Experimental photorefractive gain Γ as a function of the angle between the grating wave vector and the c-axis around ($\beta = \pi/2$)

c-axis. The beams are extraordinary polarized. We performed measurements of the gain as a function of β around $\beta = \frac{\pi}{2}$ with $k_r = 0.8\,\mu\text{m}^{-1}$ and we deduced the value of r_{42}^{T} from the slope of the experimental curve according to a procedure presented in [4]. These experiments were carried out on two crystals: BCT:Rh 1000 ppm and BCT:Rh 2000 ppm. The results are presented in Fig. 7. We found a value of 276 pm/V for the 1000-ppm rhodium-doped crystal and 215 pm/V for the 2000-ppm rhodium-doped one. Taking into account the accuracy of the measurement, these values are in good accordance with the value of 250 pm V^{-1} measured on BCT:Rh 100 ppm at 532 nm [4].

1.5 Discussion

The aim of these experiments was to determine whether rhodium improves the photorefractive properties of BCT crystals at 850 nm. First, we noticed that the absorption spectra show an absorption band proportional to the quantity of rhodium introduced in the melt and that the shape of the curve is similar to the one of $BaTiO_3$:Rh. Concerning the saturation intensity, the influence of rhodium is positive. Indeed, the saturation intensity decreases from 360 mW/cm^2 for the undoped crystal to 90 mW/cm^2 for the 2000-ppm rhodium-doped sample. Nevertheless, 90 mW/cm^2 is still a high value compared to the saturation intensity obtained in $BaTiO_3$:Rh meaning that BCT:Rh will require higher power sources to be operated. The results concerning the effective trap density are surprising. First, the effective trap density of the undoped crystal is very high. Second, the effective trap density is the same for all BCT crystals with rhodium doping from 200 to 2000 ppm, with iron doping and without doping. The first point might indicate that a photorefractive impurity is present in large amount in the undoped crystal and is responsible for the large effective trap density. The second point might indicate that the quantity of this impurity is so large that it offsets the influence of rhodium on the effective trap density. It was also noted that the effective trap density of the undoped crystal was very large at 515 nm [11]. Furthermore, we pointed out that the absorption spectrum of the undoped crystal was proportional to the one of the iron-doped crystal, so that the impurity contained in the BCT crystals might be iron. Nevertheless, this point is not clear and to have a better understanding, we will now try to modelize the charge transport in BCT:Rh at 850 nm.

2 Charge-transport situation

Modelization of the charge transport is of prime importance as it enables the tailoring of the material properties, and will allow the future growth of optimized samples that will meet the requirements of the different applications.

2.1 The two-level model with three charge states of rhodium is not valid

Different characteristic features of $BaTiO_3$:Rh can be found in BCT:Rh. For example, the absorption spectra for BCT:Rh and $BaTiO_3$:Rh are similar, with a large absorption band around 600 nm, which is attributed to rhodium. In the case of rhodium doping in $BaTiO_3$, it has been established that a two-level model with three charge states of rhodium applies [1, 2]. Furthermore, the one-level model is dismissed by the dependence of the effective trap density on the intensity. It is thus natural to consider that BCT:Rh follows a two-center model with three charge states of rhodium, like $BaTiO_3$:Rh.

As BCT is close to $BaTiO_3$, we use the results obtained on $BaTiO_3$:Rh as starting point. A complete study of $BaTiO_3$:Rh was performed by Huot [2] at 1.06 μm. He determined the parameters of the model for $BaTiO_3$:Rh at this wavelength:

- the total amount of rhodium in a 1000-ppm rhodium-doped sample and the different parameters related to Rh^{4+} and Rh^{5+}
- the photo-ionisation cross-sections,
- the recombination rates,
- the thermal emission rates.

Among these parameters, only the photo-ionisation cross-sections depend on the wavelength. To determine their values at 850 nm, we performed measurements on $BaTiO_3$:Rh at 850 nm using the same experimental procedure and the same samples as in [2]. The determined photo-ionisation cross-section of Rh^{4+} and Rh^{5+} at 850-nm rhodium parameters for $BaTiO_3$:Rh at 850 nm are given in Table 3 (second column).

This set of parameters was a basis to begin our simulations on BCT:Rh. We simulated numerically the dependence of the gain on the grating spacing for several amounts of rhodium (200 ppm, 1000 ppm and 2000 ppm) according to a two-level model with three charge states of rhodium. To estimate the total quantity of rhodium in the crystals, we assumed that it was proportional to the amount of rhodium

Table 3. Set of parameters found to fit the experimental results in the case of a three-level model. The parameters of $BaTiO_3$:Rh determined at 850 nm according to a two-level model with three charge states of rhodium are presented for comparison

Parameters	Adjusted value for BCT:Rh	Adjusted value for $BaTiO_3$:Rh
Photo-ionization cross-section of Rh^{5+}:S^+ (m^2)	9×10^{-21}	1.24×10^{-21}
Photo-ionization cross-section of Rh^{4+}:S^- (m^2)	0.4×10^{-21}	0.56×10^{-21}
Photo-ionization cross-section of Fe^{4+}:S_F (m^2)	0.001×10^{-21}	–
Recombination rate of Rh^{4+} (m^3/s):γ_+	2.92×10^{-14}	3.5×10^{-14}
Recombination rate of Rh^{3+} (m^3/s):γ_-	$15 \times \gamma_+$	$1.5 \times \gamma_+$
Recombination rate of Fe^{3+} (m^3/s):γ_F	γ_+	–
Thermal emission rate of Rh^{5+} (s^{-1}):β^+	2.3	2.3
Thermal emission rate of Rh^{4+} (s^{-1}):β^-	0.0001	0.01
Thermal emission rate of Fe^{4+} (s^{-1}):β_F	0.000125	–
Total iron concentration (m^{-3}):N_F	64×10^{23}	–
Compensation density (m^{-3}):N_{da}	0.82×10^{23}	–
Total concentration of rhodium for a 1000-ppm doped sample (m^{-3}):N_T	3.3×10^{23}	3.3×10^{23}

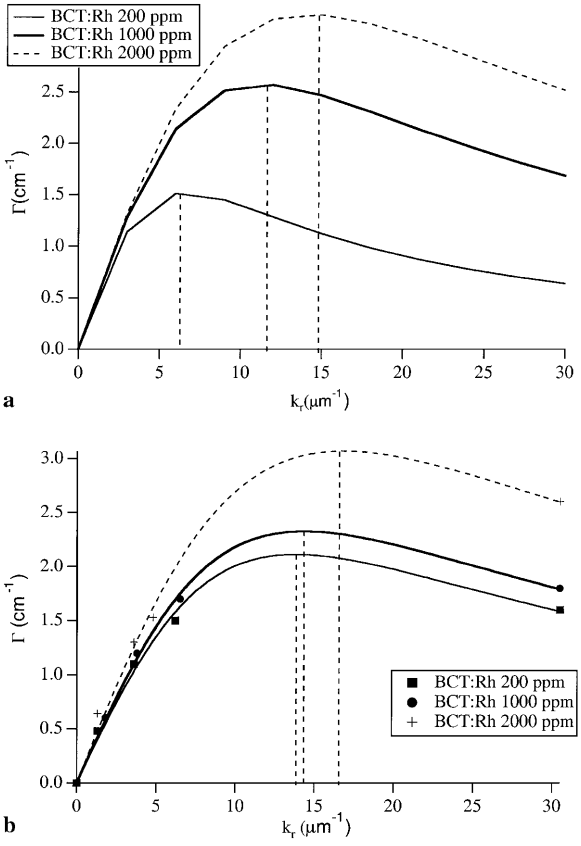

Fig. 8. a Effect of the variation of the amount of rhodium on the effective trap density in BCT:Rh, calculated according to a two-level model with three charge states of rhodium. **b** Experimental dependence of the effective trap density on the amount of rhodium in BCT:Rh. The *experimental points* are represented as well as the *fitting curves* (the fit procedure is explained in Sect. 1.4.2). In both figures, the *vertical lines* show the maximum of the curves from which we deduce the effective trap density

in the melt. Furthermore, we supposed that the quantity of rhodium that entered a crystal of BCT was the same as for a crystal of $BaTiO_3$. As the rhodium parameters for BCT:Rh might be slightly different from the ones of $BaTiO_3$:Rh, we then varied each parameter around its initial value. But, whatever the parameters we chose, simulations always indicated a variation of the effective trap density with rhodium doping (Fig. 8a) that is much larger than the one observed experimentally (Fig. 8b). Indeed, comparing Fig. 8a and b, we see that the variation of the effective trap density (which corresponds to the variation of the position of the maximum of the curves) induced by a variation of the concentration of rhodium is much lower experimentally (13–17 μm^{-1}) than on the simulated curves (7–15 μm^{-1}).

Therefore, it seems that a two-level model with three charge states of rhodium cannot explain the photorefractive effect in BCT:Rh. This point is confirmed by the fact that the undoped and iron-doped samples are sensitive at 850 nm and they exhibit the same large effective trap density as the rhodium-doped samples. Indeed, it should indicate that an impurity is present in these crystals in large amounts and is responsible for the photorefractive effect at this wavelength. As the effective trap density in the rhodium-doped samples is independent of the quantity of rhodium and is the same as in the undoped and iron-doped crystals, it seems possible that the same impurity is responsible for the photorefractive effect in all crystals. Several points tend to indicate that this impurity might be iron. First, the absorption spectra of the undoped and iron-doped samples are proportionnal, as mentionned in Sect. 1.1. Then, EPR measurements made at the University of Osnabrück indicated the presence of a large amount of iron in the rhodium-doped crystals [12]. Finally, it is well known that $BaTiO_3$:Rh contains iron as major native impurity. But, contrary to the case of $BaTiO_3$:Rh, where the presence of iron was neglected, it seems here necessary to take it into account to modelize the photorefractive effect in BCT:Rh. Indeed, the amount of iron in the BCT crystals seems to be much larger than in the $BaTiO_3$ crystals. It might be due to the growth temperature, which is 200 °C higher for BCT, that favors the incorporation of iron in the crystal. That is why we think that the photorefractive model that best explains the photorefractive properties of BCT:Rh is a three-level model with two levels of rhodium and one level of iron.

2.2 *Charge-transport model in* BCT:Rh

Here we briefly present the three-level model and the simulations, which have given a good accordance between the model and the experimental results.

2.2.1 Description of the three-level model. We consider a three-level model with two levels of rhodium ($Rh^{3+/4+}$, $Rh^{4+/5+}$) and one level of iron ($Fe^{3+/4+}$). When the crystal is illuminated, we have the following charge transfers:

$$\begin{cases} Rh^{5+} \leftrightarrow Rh^{4+} + \text{hole} \\ Rh^{4+} \leftrightarrow Rh^{3+} + \text{hole} \\ Fe^{4+} \leftrightarrow Fe^{3+} + \text{hole} \ . \end{cases} \quad (9)$$

We consider Rh^{4+} and Fe^{4+} as neutral states of charges and we denote them respectively as N and N_F. Then Rh^{3+} and Fe^{3+} can be considered as recombination centers and Rh^{5+} as a generation center for holes. Their densities are respectively

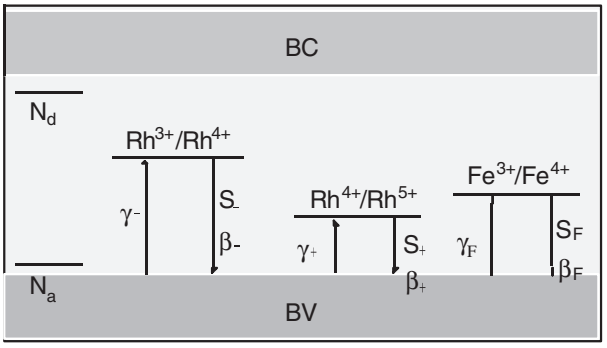

Fig. 9. Schematic energy level diagram of BCT:Rh containing iron as an impurity

N^-, N_F^-, and N^+. The electrical neutrality of the crystal is achieved by shallow donor and acceptor densities N_D and N_A. The compensation density is denoted as $N_{da} = N_D - N_A$. p is the density of free holes in the valence band.

A schematic diagram of the structure of the dopant levels is shown in Fig. 9.

The photo-ionization cross-sections are denoted as S, β are the thermal emission rates and γ the rates of recombination.

If N_T is the total density of rhodium and N_{TF} the total density of iron, we have:

$$\begin{cases} N_T = N^- + N + N^+ \\ N_{TF} = N_F^- + N_F \ . \end{cases} \tag{10}$$

The rate equations are:

$$\begin{cases} \frac{\partial N^-}{\partial t} = (S^- I + \beta^-)N - \gamma^- p N^- \\ \frac{\partial N^+}{\partial t} = -(S^+ I + \beta^+)N^+ + \gamma^+ p N \\ \frac{\partial N_{F^-}}{\partial t} = (S_F I + \beta_F)N_F - \gamma_F p N_F^- \ . \end{cases} \tag{11}$$

The current density and the continuity equation for holes are:

$$\mathrm{div}\boldsymbol{j} = e\frac{\partial(N_{da} + p + N^+ - N^- - N_F^-)}{\partial t} \tag{12}$$

$$\boldsymbol{j} = ep\mu\boldsymbol{E} - \mu k_B T \nabla p \ . \tag{13}$$

Poisson's equation relates the electric field to the charge densities:

$$\mathrm{div}\boldsymbol{E} = \frac{e}{\varepsilon}(N_{da} + p + N^+ - N^- - N_F^-) \ . \tag{14}$$

Then, we perform a classical resolution of these equations under an interference pattern illumination $I = I_0 + \frac{1}{2}(m.I_0 e^{ikx} + \text{c.c.})$ (with I_0 the total incident illumination and m the modulation of the fringes). We write each quantity as $Q = Q_0 + \frac{1}{2}(Q_1 e^{ikx} + \text{c.c.})$, and linearize the equations, to obtain two sets of equations. The "zeroth-order" set relates the space-invariant quantities Q_0 to I_0. The "first-order" set defines the amplitude of the induced space-charge field as a function of the modulation of the fringes. The sets are then solved numerically and we calculate the photorefractive gain as a function of the grating spacing and the pump intensity to compare with the experimental results.

2.2.2 Determination of the initial parameters. The following parameters are necessary for the simulations:

– rhodium parameters: the photo-ionisation cross-sections S^+ and S^-, the thermal ionization rates β_+ and β_-, the recombination rates γ^+ and γ^- and the total density of rhodium N_T.
– iron parameters: the photo-ionisation cross-section S_F, the thermal ionization rate β_F, the recombination rate γ_F and the total density of iron N_{TF}.
– the compensation density N_{da}.

For all the following numerical simulations, we assumed that the Fermi level did not change with rhodium doping. So N_{da} was considered as a constant in all the crystals.

For the rhodium parameters, we used as initial values the $BaTiO_3$:Rh ones determined at 850 nm (Table 3, second column).

To determine the iron parameters, we used the experimental results on the undoped crystal. Indeed, we considered that the photorefractive effect in this crystal was only due to iron. We simulated a charge-transport model with one center ($Fe^{3+/4+}$). The initial values of the parameters were chosen according to [13], which gives indications about parameters for the iron level in $BaTiO_3$:Rh: β_F might be of the order of $5 \times 10^{-4}\ s^{-1}$, S_F might be small compared to S^- and γ_F is not given and will be taken as equal to γ^+ in $BaTiO_3$:Rh (Table 3, second column). By adjusting the simulated curves to the experimental results, we obtained much information about the values of the parameters. First, the dependence of the gain with intensity allowed us to determine precisely the parameters S_F and β_F. Second, the value of the effective trap density gave us a minimum value for the quantity of iron contained in the crystal. Indeed, in the case of a one-center model, we have:

$$N_{eff} = N_F^- - \frac{N_{da}^2}{N_{TF}} = N_{da}\frac{N_{TF} - N_{da}}{N_{TF}} \tag{15}$$

which can be written:

$$N_{da}^2 - N_{TF}N_{da} + N_{eff}N_{TF} = 0 \tag{16}$$

To have a solution of this second-order equation, we should have: $N_{TF}(N_{TF} - 4N_{eff}) \geq 0$ which corresponds to $N_{TF} \geq 4N_{eff}$.

And, knowing the value of the effective trap density ($6 \times 10^{22}\ m^{-3}$), we have $N_{TF} \geq 24 \times 10^{22}\ m^{-3}$.

When the value of N_{TF} was fixed, we obtained two values for the compensation density N_{da}: one is of the same order of magnitude as N_{TF} and the other is small compared to N_{TF}. Simulations showed that it is better to choose the smaller one according to experimental results.

2.2.3 Numerical simulations. With this initial set of parameters, we performed numerical simulations simultaneously on the undoped and rhodium-doped samples for several amounts of rhodium (200, 370, 600, 1000 and 2000 ppm). Our aim was to find a set of parameters which enabled us to explain our experimental results. To do this, we varied the parameters around their initial values to improve the accordance between simulated curves and experimental ones. It was possible to find a convenient set

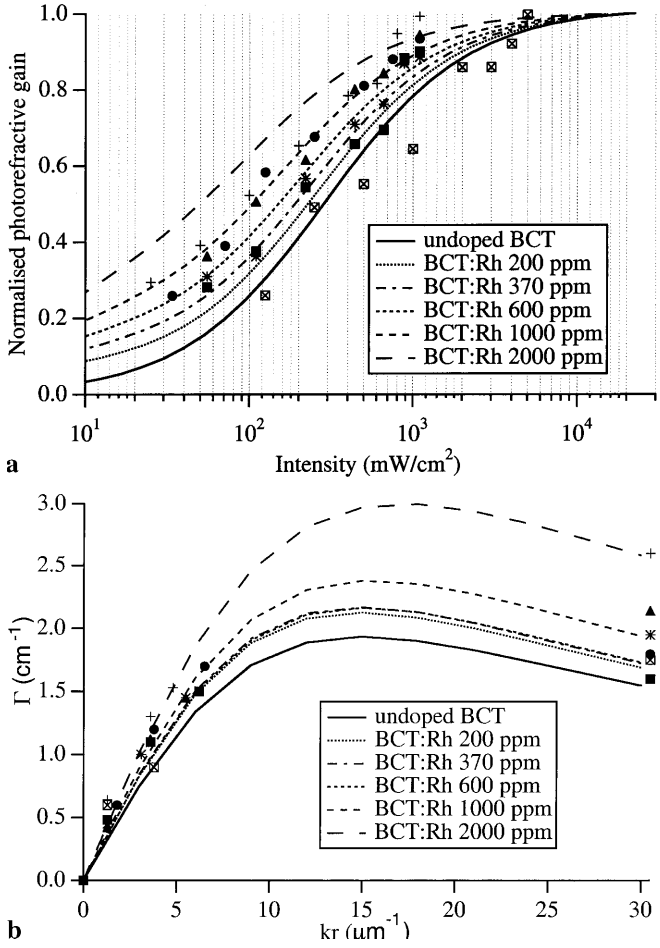

Fig. 10a,b. Comparison between experimental points and simulated curves with simulations accordingto a three-level model with two levels of rhodium and one level of iron. Concerning the simulated curves of the gain as a function of the grating wave vector, we use in the calculations the value of r_{22}^{eff} experimentally determined for each crystal (see Table 1). **a** represents the dependence of the normalized gain with intensity and **b** concerns the dependence of the gain with the grating spacing. ⊠ undoped BCT; ■ BCT:Rh 200 ppm; ✳ BCT:Rh 370 ppm; ▲ BCT:Rh 600 ppm; ● BCT:Rh 1000 ppm; + BCT:Rh 2000 ppm

of parameters (Table 3, first column) so that the simulated curves were in good accordance with the experimental results (Fig. 10). Figure 10a represents the dependence of the gain on intensity. The experimental points and the simulated curves are represented. We consider that we obtained a good accordance because a slight variation of some parameters induces a large translation of the curves. In Fig. 10b, we have represented the dependence of the gain with the grating spacing. The lines corresponds to simulations and we see that they are in good accordance with the experimental points.

2.3 Validity of the model

Considering the number of unknown parameters, this set is certainly not the only one existing but the values found seem to make sense. First, the values obtained for the rhodium parameters in BCT are not far from the ones obtained for $BaTiO_3$:Rh at the same wavelength. Second, the large amount of iron that is found in BCT crystals is in good accordance with results obtained at the University of Osnabrück [12]. Moreover, it enables us to explain the independence of the effective trap density on rhodium and iron doping. Indeed, it seems that the quantity of dopant added (rhodium or iron) is negligible compared to the amount of iron already present in the crystals because it does not change the effective trap density. But this point has to be further studied.

3 Comparison of BCT:Rh with $BaTiO_3$:Rh

BCT:Rh is a good photorefractive material. Most of its photorefractive properties are not far from the ones of $BaTiO_3$:Rh.

The electro-optic coefficient r_{42}^{T} is really smaller than in $BaTiO_3$ but it still has a value that should be sufficient for applications such as phase conjugation. The ordinary photorefractive gain is of the same order of magnitude in both crystals. Indeed, the gain measured in a 2000-ppm $BaTiO_3$:Rh (labeled X15) at 850 nm in a symmetrical configuration, with ordinary polarizations and for a grating wave vector of 3.6 μm^{-1} is around 1.1 cm^{-1}, whereas it is around 1.3 cm^{-1} in a 2000-ppm BCT:Rh (Fig. 4b).

The smallest response time is measured for a 2000-ppm rhodium-doped BCT with counterpropagating waves and was around 3 s for an intensity of 1 W cm^{-2}. To compare results with those of $BaTiO_3$:Rh, we measured 8 s for a 2000-ppm BCT:Rh with a grating wave vector of 4 μm^{-1} for $I = 1$ W cm^{-2}. In a 2000-ppm $BaTiO_3$:Rh (labeled Y32-B), we measured $\tau = 60$ s for $I = 600$ mW cm^{-2} for the same grating spacing and the same wavelength. As the response time in $BaTiO_3$:Rh is proportionnal to I^{-1}, we should have a response time of 36 s for $I = 1$ W cm^{-2}. Thus the response time is better in BCT:Rh than in $BaTiO_3$:Rh for the same amount of rhodium.

The saturation intensity is the unique parameter that differs a lot between both crystals. It is 100 to 1000 times higher in BCT:Rh than in $BaTiO_3$:Rh due to the influence of iron.

4 Conclusion

BCT:Rh crystals are sensitive in the infrared at 850 nm. Rhodium doping improves this sensitivity in term of saturation intensity but the obtained saturation intensities are still very high compared to the ones of $BaTiO_3$:Rh. Moreover, rhodium doping up to 2000 ppm does not improve the effective trap density. It might be due to the presence of a large amount of iron in the crystals. Indeed, to explain the experimental results, we need to take into account the presence of iron in our charge-transport model. Iron seems to be responsible for the high saturation intensity, what can be a drawback for some applications. To improve this characteristic of the BCT:Rh crystals, the next step in the development will be to test crystals doped with a larger amount of rhodium.

Acknowledgements. Valuable discussions with D. Rytz, O.F. Schirmer and G. Malovichko are gratefully acknowledged.

References

1. H. Kröse, R. Scharfschwerdt, O.F. Schirmer, H. Hesse: Appl. Phys. B **61**, 1 (1995)
2. N. Huot, J.M.C. Jonathan, G. Roosen: Appl. Phys. B **65**, 486 (1997)
3. C. Kuper, K. Buse, U. Van Stevendaal, M. Weber, T. Leidlo, H. Hesse, E. Krätzig: Ferroelectrics **208–209**, 213 (1998)
4. S. Bernhardt, P. Delaye, H. Veenhuis, G. Roosen: Appl. Phys. B **70**, 789 (2000)
5. H. Veenhuis, T. Börger, K. Peithmann, M. Flaspöhler, K. Buse, R. Pankrath, H. Hesse, E. Krätzig: Appl. Phys. B **70**, 797 (2000)
6. B.A. Wechsler, M.B. Klein, C.C. Nelson, R.N. Schwartz: Opt. Lett. **19**, 8 (1994)
7. P. Delaye, L.A. de Montmorillon, I. Biaggio, J.C. Launay, G. Roosen: Opt. Commun. **134**, 580 (1997)
8. K. Buse: Appl. Phys. B **64**, 273 (1997); K. Buse: Appl. Phys. B **64**, 391 (1997)
9. F.P. Strohkendl, J.M.C. Jonathan, R.W. Hellwarth: Opt. Lett. **11**, 5 (1986)
10. N.V. Kukhtarev, V.B. Markov, S.G. Odulov, M.S. Soskin, V.L. Vinetskii: Ferroelectrics **22**, 949 (1979)
11. H. Veenhuis, T. Börger, K. Buse, C. Kuper, H. Hesse, E. Krätzig: J. Appl. Phys. **88**, 1042 (2000)
12. O.F. Schirmer: private communication
13. L. Corner, R. Ramos-Garcia, A. Petris, M.J. Damzen: Opt. Commun. **143**, 165 (1997)